Inorganic Chemistry

Article

pubs.acs.org/IC

African Viper Poly-His Tag Peptide Fragment Efficiently Binds Metal Ions and Is Folded into an α-Helical Structure

Joanna Watly,[†] Eyal Simonovsky,[‡,§] Nuno Barbosa,[†] Marta Spodzieja,[∥] Robert Wieczorek,[†] Sylwia Rodziewicz-Motowidlo,[∥] Yifat Miller,*[,‡,§] and Henryk Kozlowski*[,†]

[†]Faculty of Chemistry, University of Wrocław, 50-383 Wrocław, Poland

[‡]Department of Chemistry and [§]Ilse Katz Institute for Nanoscale Science and Technology, Ben-Gurion University of the Negev, Beer-Sheva 84105, Israel

[∥]Faculty of Chemistry, University of Gdańsk, 80-308 Gdańsk, Poland

Supporting Information

ABSTRACT: Snake venoms are complex mixtures of toxic and often spectacularly biologically active components. Some African vipers contain polyhistidine and polyglycine peptides, which play a crucial role in the interaction with metal ions during the inhibition of snake metalloproteases. Polyhistidine peptide fragments, known as poly-His tags, play many important functions, e.g., in metal ion transport in bacterial chaperon proteins. In this paper, we report a detailed characterization of Cu^{2+}, Ni^{2+}, and Zn^{2+} complexes with the EDDHHHHHHHHHG peptide fragment (pHG) derived from the venom of the rough scale bush viper (*Atheris squamigera*). In order to determine the thermodynamic properties, stoichiometry, binding sites, and structures of the metal−pHG complexes, we used a combination of experimental techniques (potentiometric titrations, electrospray ionization mass spectrometry, UV−vis spectroscopy, circular dichroism spectroscopy, and electron paramagnetic resonance spectroscopy) and extensive computational tools (molecular dynamics simulations and density functional theory calculations). The results showed that pHG has a high affinity toward metal ions. The numerous histidine residues located along this sequence are efficient metal ion chelators with high affinities toward Cu^{2+}, Ni^{2+}, and Zn^{2+} ions. The formation of an α-helical structure induced by metal ion coordination and the occurrence of polymorphic binding states were observed. It is proposed that metal ions can "move along" the poly-His tag, which serves as a metal ion transport pathway. The coordination of Cu^{2+}, Ni^{2+}, and Zn^{2+} ions to the histidine tag is very effective in comparison with other histidine-rich peptides. The stabilities of the metal−pHG complexes increase in the order $Zn^{2+} < Ni^{2+} \ll Cu^{2+}$.

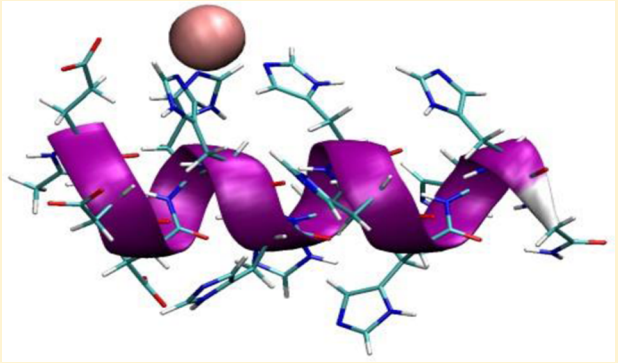

INTRODUCTION

Polyhistidine (poly-His) tags are peptides that consist of multiple histidine residues, which can efficiently bind metal ions.[1] Poly-His tags are used in molecular biology for protein purification in a procedure in which their multiple histidines play a role in binding metal ions.[2] Poly-His motifs have been found in several metal transporters, prion proteins, and domains of bacterial chaperones responsible for Ni^{2+} homeostasis.[3] Histidine repeats are found also in Zn-finger domains that have been implicated in interactions between nucleic acids and proteins, and a His stretch has been described as a protein-interacting surface of the transcriptional regulator cyclin T1.[4] One of the most interesting families of histidine-rich natural peptides are poly-His−poly-Gly peptides, found in African snake venoms.[5] Poly-His sequences in these natural peptides and proteins have polymorphic binding states.[1,6] Therefore, we propose that the metal ions can bind to different sites in poly-His tags and also "move back and forth" along such regions, forming polymorphic states. Such a process in which metal ions are transported can be of great biological importance—the transport of nickel ions between different poly-His domains of Ni^{2+} chaperones in bacteria can serve as a good example.

The families of natural peptides that have been found in the African viper *Atheris squamigera* are poly-His−poly-Gly peptides having the sequence $EDDH_9GVG_{10}$ (pHpG-1).[5] These peptides consist of nine consecutive His residues and 10 consecutive Gly residues. It has been proposed that these families of pHpG-1 peptides may protect against snake-venom-inhibiting proteolysis by some of the proteins of the snake venom. The specific role of the nine His residues is unknown; what is certain is that these nine His residues have the ability to bind metal ions, as previously shown for the shorter His_6 tag.[1] Because of their ability to bind metals (e.g., Cu^{2+}, Ni^{2+}, or

Received: February 27, 2015
Published: July 27, 2015

DOI: 10.1021/acs.inorgchem.5b01029
Inorg. Chem. 2015, 54, 7692−7702

Zn^{2+}), it is likely that these families of peptides may play a key role in the interaction with metal ions and consequently in the inhibition of snake metalloproteases.[5,7] Our previous studies have shown that the full sequence of the pHpG-1 peptide[6] binds metal ions more efficiently than the shorter His_6 tag (Ac-HHHHHH-NH_2).[1] It was proposed that increasing the length of the His-rich chain increases the efficiency of metal ion binding. In the present work, we examined the binding efficiency and the structural features of metal ions that bind to the short protected fragment of pHpG-1, namely, Ac-EDDH_9G-NH_2 (pHG). We further investigated the structural differences and binding efficiencies for various types of metal ions (Cu^{2+}, Ni^{2+}, and Zn^{2+}) in the metal−pHG complexes using various experimental and computational tools.

EXPERIMENTAL SECTION

Materials. Ac-EDDHHHHHHHHHG-NH_2 (pHG) was synthesized by solid-phase peptide synthesis (SPPS) with a semiautomated peptide synthesizer (Millipore 9050 Plus PepSynthesizer, Millipore Corporation, Burlington, VT, USA) using general SPPS conditions.[8,9] The synthesis was performed on TentaGel R RAM resin (0.19 mmol/g) using 9-fluorenylmethoxycarbonyl/*tert*-butyl (Fmoc/tBu) chemistry with the following side-chain-protected amino acid derivatives: Fmoc-Glu(OtBu)-OH, Fmoc-Asp(OtBu)-OH, Fmoc-His(Trt)-OH, Fmoc-Gly-OH. Acetylation of the N-terminal amino group of the peptide was performed using 1-acetylimidazole (1.10 g/1 g of resin at room temperature for 24 h). The peptide was cleaved from the resin for 2 h using a mixture of 88% trifluoroacetic acid (TFA), 5% phenol, 5% deionized water, and 2% triethylsilane (10 mL/1 g of resin at room temperature for 2 h). After filtration of the exhausted resin, the solution was concentrated in vacuo, and the residue was triturated with Et_2O. The precipitated peptide was centrifuged for 15 min, followed by decantation of the ether phase from the crude peptide (this process was repeated three times). After evaporation of Et_2O, the peptide was dissolved in H_2O and lyophilized. Purification of the crude peptide was carried out using reversed-phase (RP) HPLC on a semipreparative Kromasil C8 column (250 mm × 20 mm, 5 μm). A linear gradient from 0% B to 30% B in A in 120 min was used. The aqueous system (A) consisted of 0.1% (v/v) TFA solution in water, whereas the organic phase (B) was 80% acetonitrile in water containing 0.08% (v/v) TFA. Purification was monitored by UV absorption at a wavelength of 222 nm. The purity of the peptide was verified by liquid chromatography−electrospray ionization ion trap time of flight mass spectrometry (Shimadzu, Shimpol, Warsaw, Poland) and by RP-HPLC with a Kromasil C8 analytical column (250 mm × 4.6 mm, 5 μm) employing a gradient of 0% to 100% B in A in 60 min, with A and B as described above.

Cu^{2+}, Ni^{2+}, and Zn^{2+} chlorides were extra-pure products (Sigma-Aldrich). The concentrations of stock solutions of these salts were determined by inductively coupled plamsa mass spectrometry. The carbonate-free stock solution of NaOH (0.1 mol·dm^{-3}) was purchased from Sigma-Aldrich and then potentiometrically standardized with potassium hydrogen phthalate as a primary standard. The HCl stock solution was prepared by diluting concentrated HCl (Sigma-Aldrich) and then standardized with NaOH. All of the sample solutions were prepared with freshly doubly distilled water. The ionic strength (I) was adjusted to 0.1 mol·dm^{-3} by addition of KCl (Sigma-Aldrich).

Potentiometric Measurements. Potentiometric measurements were performed at a constant temperature of 25 °C under an argon atmosphere using a Molspin pH meter equipped with a Mettler-Toledo InLab semicombined electrode and a micrometer syringe with a volume of 0.5 cm^3. Before each measurement, the electrode was calibrated by titration of HCl having a concentration of 4×10^{-3} mol·dm^{-3} with NaOH (0.1 mol·dm^{-3}).[10] Stability constants for proton, Cu^{2+}, Ni^{2+}, and Zn^{2+} complexes were calculated from potentiometric titration curves registered over the pH range 2.5−11. The pH-metric titrations were performed in an aqueous solution of HCl at 0.1 mol·dm^{-3} KCl. The titrant was a carbonate-free standard solution of NaOH. The ligand concentration was about 5×10^{-4} mol·dm^{-3}, and the metal-to-ligand ratio was 1:1.1. The exact concentrations and the purities of the ligand solutions were determined by the Gran method.[11] The HYPERQUAD and SUPERQUAD programs were used for the stability constant calculations.[12,13] Standard deviations were given by the program itself and refer to random errors only. The speciation and competition diagrams were computed with the HYSS program.[14]

Spectroscopic Studies. The absorption spectra in the UV−vis region were recorded at 25 °C on a Varian Cary 300 Bio spectrophotometer in 1 cm path length quartz cells. Circular dichroism (CD) spectra were recorded on Jasco J 715 spectropolarimeter over the 190−800 nm range using different path lengths (1, 0.1, and 0.01 cm). The concentrations of solutions used for UV−vis and CD spectroscopic studies were similar to those employed in the potentiometric experiments. Electron paramagnetic resonance (EPR) spectra were recorded in liquid nitrogen on a Bruker ELEXSYS E500 CW-EPR spectrometer at X-band frequency (9.5 GHz) and equipped with an ER 036TM NMR teslameter and an E41 FC frequency counter. The ligand pHG was prepared in an aqueous solution of HCl at I = 0.1 mol·dm^{-3} (KCl). The concentration of Cu^{2+} was 1×10^{-3} mol·dm^{-3}, and the M:L molar ratio was 1:1.1. Ethylene glycol (30%) was used as a cryoprotectant for EPR measurements. The EPR parameters were analyzed by computer simulation of the experimental spectra using WIN-EPR SIMFONIA software, version 1.2 (Bruker). The pH was adjusted with appropriate amounts of HCl and NaOH solutions.

Mass Spectrometric Measurements. High-resolution mass spectra were obtained on BrukerQ-FTMS and Bruker MicrOTOF-Q spectrometers (Bruker Daltonik, Bremen, Germany) equipped with an Apollo II electrospray ionization source with an ion funnel. The BrukerQ-FTMS spectrometer was used for measurements on Cu^{2+}−pHG complexes in the range of positive values of mass-to-charge ratio (m/z) from 150 to 1500. The instrumental parameters were as follows: scan range, m/z 400−1600; dry gas, nitrogen; temperature, 170 °C; capillary voltage, 4500 V; ion energy, 5 eV. The capillary voltage was optimized to the highest signal-to-noise ratio. Small changes in voltage (±500 V) did not significantly affect the optimized spectra. The Bruker MicrOTOF-Q spectrometer was used for measurements on Ni^{2+}−pHG and Zn^{2+}−pHG complexes in the positive ion mode over the m/z range from 200 to 1700. The instrumental parameters were as follows: scan range, m/z 250−2000; dry gas, nitrogen; temperature, 200 °C; ion source voltage, 4500 V; collision energy, 10 eV. The Cu^{2+}−pHG, Ni^{2+}−pHG, and Zn^{2+}−pHG complexes (metal:ligand stoichiometry of 1:1.1, $[ligand]_{tot} = 5 \times 10^{-4}$ mol·dm^{-3}) were prepared in a 1:1 MeOH/H_2O mixture at pH 4.5. The samples were infused at a flow rate of 3 μL/min. Before each experiment, the instrument was calibrated externally with the Tunemix mixture. Data were processed by application of the Compass DataAnalysis 4.0 program (Bruker Daltonik).

Protocol for Molecular Dynamics Simulations. The 12 models were first minimized as we have done previously for amyloids and other peptides.[15−21] The molecular dynamics (MD) simulations of the solvated models were performed in the *NPT* ensemble using NAMD[22] with the CHARMM27 force field.[23,24] The standard force field available in NAMD is not applicable to the computation of metal−peptide or metal−protein complexes. We previously developed force-field parameters for the divalent ions Cu^{2+} and Zn^{2+} ligated to various amino acids. This new force field has been extensively used for metal−peptide complexes[1,6,25,26] and metal−protein complexes.[16,27] Each model was energy-minimized and explicitly solvated in a TIP3P water box[28,29] with a minimum distance of 15 Å from each edge of the box. Each water molecule within 2.5 Å of the model was removed. Counterions were added at random locations to neutralize the model's charge. The Langevin piston method[30,31] with a decay period of 100 fs and a damping time of 50 fs was used to maintain a constant pressure of 1 atm. A temperature of 310 K was controlled by a Langevin thermostat with a damping coefficient of 10 ps.[22] The short-range van der Waals interactions were calculated using a switching function with a twin range cutoff of 10.0 and 12.0 Å. Long-range electrostatic

DOI: 10.1021/acs.inorgchem.5b01029
Inorg. Chem. 2015, 54, 7692−7702

Table 1. Potentiometric and Spectroscopic Data for Proton and Cu^{2+}−pHG Complexes in an Aqueous Solution of HCl at 0.1 mol·dm^{-3} KCl[a]

				UV−vis		CD		EPR		
species	log β	pK_a	proposed donors	λ/nm	ε/M^{-1} cm^{-1}	λ/nm	$\Delta\varepsilon$/M^{-1} cm^{-1}	$A_{\parallel}$ (A_{zz})/G	$g_{\parallel}$ (g_z)	$g_{\perp}$ ($g_x = g_y$)
HL	7.98(1)	7.98								
H_2L	14.96(1)	6.98								
H_3L	21.90(1)	6.94								
H_4L	28.06(2)	6.16								
H_5L	34.21(2)	6.15								
H_6L	39.72(1)	5.51								
H_7L	45.04(1)	5.32								
H_8L	49.60(1)	4.56								
H_9L	53.30(1)	3.70								
$H_{10}L$	56.04(2)	2.74								
$H_{11}L$	58.54(2)	2.50								
CuH_6L	45.75(2)		$2N_{im}$	640	37.1	578	−0.22			
CuH_5L	41.56(3)	4.19	$3N_{im}$	605	65.5			175.4	2.26	2.047
CuH_4L	37.36(3)	4.20	$3N_{im}$	605	65.5	624	−0.24			
						522	0.39			
						320	−0.13			
CuH_3L	32.14(4)	5.22	$3N_{im}$, N^-	568	69.9	644	−0.31	190.7	2.24	2.046
				313	239.0	530	1.14			
						317	−0.71			
CuH_2L	26.62(4)	5.52	$3N_{im}$, N^-	564	70.0	644	−0.35			
				313	239.0	531	1.40			
						317	−0.88			
CuHL	20.11(4)	6.51	$3N_{im}$, N^-	564	72.0	644	−0.36	191.7	2.24	2.047
				313	246.0	531	1.44			
						317	−0.89			
CuL	13.37(5)	6.74	$3N_{im}$, N^-	564	77.0	644	−0.33	191.7	2.24	2.047
				313	272.0	531	1.38			
						319	−0.85			
$CuH_{-2}L$	−2.93(6)		$2N_{im}$, $2N^-$	562	107.0	628	0.47	187.5	2.23	2.048
						539	−0.31			
						486	0.19			
						425	0.04			
						399	0.07			
						339	−1.35			
$CuH_{-3}L$	−11.72(8)	8.79	N_{im}, $3N^-$	536	116.7	648	0.91	194.9	2.19	2.048
						517	−1.10			
						399	0.01			
						344	−0.61			

[a] $[Cu^{2+}] = 4 \times 10^{-4}$ mol·dm^{-3} for potentiometry, UV−vis, and CD measurements at 25 °C. $[Cu^{2+}] = 1 \times 10^{-3}$ mol·dm^{-3} for EPR measurements at 77 K in water/ethylene glycol solution. The Cu^{2+}:ligand ratio was 1:1.1.

interactions were calculated using the particle mesh Ewald method with a cutoff of 12.0 Å.[32,33] The equations of motion were integrated using the leapfrog integrator with a step size of 1 fs. The solvated systems were energy-minimized for 2000 conjugate-gradient steps, where the hydrogen-bonding distance between the β-sheets in each oligomer was fixed in the range 2.2−2.5 Å. The counterions and water molecules were allowed to move. The hydrogen atoms were constrained to the equilibrium bond length using the SHAKE algorithm.[34] The minimized solvated systems were energy-minimized for 5000 additional conjugate-gradient steps and 20 000 heating steps at 250 K, with all atoms being allowed to move. Then the system was heated from 250 to 310 K for 300 ps and equilibrated at 310 K for 300 ps. All of the simulations were run for 30 ns at 310 K. Parametrizations for the Cu^{2+}−peptide complexes were performed for all of the MD simulations. The force constant values for Cu^{2+}−N atom and Cu^{2+}−O atom interactions were in the range of 10−50 kcal/mol^2. Along the MD simulations the Cu^{2+} binds to two His residues.

Generalized Born Method with Molecular Volume. Relative conformational energies can be compared only for models that have the same sequence and number of peptides, and thus, the relative conformational energies were computed for all 12 models. To obtain the relative conformational energies of the 12 models, the last 5 ns of each model's trajectory (a total of 500 conformations) was first extracted from the explicit MD simulation excluding the water molecules. The solvation energies for all of the conformations were calculated using the generalized Born method with molecular volume (GBMV).[35,36] In the GBMV calculations, the dielectric constant of water was set to 80. The hydrophobic solvent-accessible surface area (SASA) term factor was set to 0.00592 kcal mol^{-1} Å^{-1}. Each conformation was minimized using 1000 cycles, and the conformational energy was evaluated by grid-based GBMV.

A total of 6000 conformations (500 for each model) were used to construct the energy landscape of the 12 models and to evaluate the conformer probabilities using Monte Carlo (MC) simulations. In the first step, two conformations i and j were randomly selected. Then the Boltzmann factor was computed as $e^{-(E_j-E_i)/kT}$, where E_i and E_j are the conformational energies evaluated using the GBMV calculations for conformations i and j, respectively, k is the Boltzmann constant, and T

DOI: 10.1021/acs.inorgchem.5b01029
Inorg. Chem. 2015, 54, 7692−7702

is the absolute temperature (298 K used here). If the value of the Boltzmann factor was larger than the random number, then the move from conformation i to conformation j was allowed. After 1 million steps, the conformations "visited" for each model were counted. Finally, the relative probability of model n was evaluated as $P_n = N_n/N_{total}$, where P_n is the population of model n, N_n is the total number of conformations visited for model n, and N_{total} is the total number of steps. The advantages of using MC simulations to estimate conformer probabilities lie in their good numerical stability and the control of transition probabilities among several conformers that they allow. Using the 6000 conformations generated from the MD simulations (500 for each of the 12 models), we estimated the overall stability and populations for each conformer, with the energy landscape being computed with GBMV for these 12 models. The group of these 12 models may be only a very small percentage of the ensemble. Nevertheless, the carefully selected models cover the most likely structures.

Dictionary of Secondary Structure of Proteins and Structural Identification Algorithms. The Dictionary of Secondary Structure of Proteins (DSSP) algorithm is the standard method for assigning secondary structure to the amino acids of a protein or a peptide given the atomic-resolution coordinates of the protein or peptide. It does this by reading the positions of the atoms in a protein (the ATOM records in a Protein Data Bank file) and calculating the hydrogen-bonding energies between all atoms. The best two hydrogen bonds for each atom are then used to determine the most likely class of secondary structure for each residue in the protein or peptide. We applied the DSSP algorithm that is embedded in the CHARMM software.[37] The DSSP algorithm provides information on specific domains that illustrate α-helix and β-sheet structures. It does not distinguish between various types of helix, such as 3_{10} helix, α-helix, etc. To obtain information on the type of α-helix, we applied the Structural Identification (STRIDE) algorithm[38] that is embedded in VMD.[39]

Density Functional Theory Calculations. Quantum-chemistry methods are useful tools to predict the structure and stability of complexes.[40−42] Molecular orbital calculations on complexes of Cu^{2+}, Ni^{2+}, and Zn^{2+} with pHG (1:1 ratio) were performed using density functional theory (DFT). The three different initial structures of the free pHG peptide for the DFT calculations were generated on the basis of the amino acid sequence after an 85 ps simulation at 300 K without cutoffs using BIO+, which is implemented in the CHARMM force field. All of the calculations were performed with the Gaussian 09[43] suite of programs using the M06 hybrid functional[44] and the 6-311G basis set. To obtain a preliminary estimate the energy difference between two types of two bonding His, we examined two model Cu^{2+} complexes with the Ac-$(His)_3$-NH_2 peptide. In the first model, the metal ion was connected to two neighboring His residues (His1 and His2), and in the second model, the metal ion was connected to non-neighboring His residues (His1 and His 3). The second model showed higher stability than the first model (the energy difference was 4.22 kcal/mol, which is a typical energy for a hydrogen bond). We therefore expect that in the folded stable Cu^{2+}−pHG complex the metal ion can bind to neighboring His residues (His_n and His_{n+1}) and to non-neighboring His residues (His_n and His_{n+2}).

RESULTS AND DISCUSSION

Protonation Constants of the pHG Peptide and Stability Constants of the Cu^{2+}−pHG Complexes. The pHG peptide contains 12 possible sites of protonation, 11 of which were in the detection scope of our electrode. Among these 11 sites, nine are assigned to the nine histidine residues and the other two to the acidic residues (Table 1). The pK values obtained from the potentiometric data are in good agreement with those found in the literature for similar poly-His systems.[1,6] The ligand is completely deprotonated at pH 10 (Figure S1 in the Supporting Information).

To investigate the structural and thermodynamic properties of Cu^{2+}−pHG complexes, we applied electrospray ionization mass spectrometry (ESI-MS), potentiometric titrations, and CD and EPR spectroscopy at different pH values. The ESI-MS measurements revealed the stoichiometry of the metal complexes, indicating that only equimolar species were present under the studied conditions (Figure S2). pHG forms equimolar complexes with Cu^{2+} at m/z 886.3 (for $[CuL]^{2+}$) and at m/z 591.2 (for $[CuL]^{3+}$). The experimental and simulated signals showed excellent agreement between the calculated and experimental data. According to potentiometric data calculations, Cu^{2+} forms nine species with pHG characterized by the log β and pK_a values collected in Table 1. The distribution diagram for the obtained Cu^{2+}−pHG complexes is shown in Figure 1.

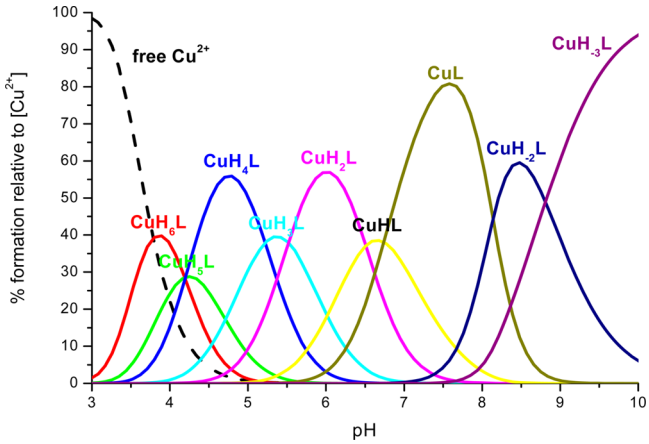

Figure 1. Representative distribution diagram for the formation of Cu^{2+}−pHG complexes at 25 °C and I = 0.1 mol·dm^{-3} (KCl). $C^{\circ}_M = 4 \times 10^{-4}$ mol·dm^{-3}; M:L molar ratio = 1:1.1.

The EPR parameters ($A_{\parallel}$ = 120.6 G and $g_{\parallel}$ = 2.42) at pH 3.18 (Figure S3) are in agreement with the Peisach−Blumberg ($A_{\parallel}$ vs $g_{\parallel}$) plot for four oxygen donors.[45] The first complex detected at low pH is CuH_6L with a maximum concentration at pH 3.9 (Figure 1). It is most probable that in this complex two imidazole residues are coordinated to Cu^{2+}, although binding to the carboxylate group can also be possible. The coordination of Cu^{2+} to two imidazole nitrogens (N_{im}) is supported by the d−d band at 640 nm for pH 3.7 (Figure 2). The corresponding value of 6.03 for log K*, which refers to the reaction $Cu^{2+} + H_6L \rightleftarrows CuH_6L$ [log K* = log $\beta(CuH_6L)$ − log $\beta(H_6L)$], also suggests the involvement of two imidazole rings in copper coordination in this system.[46] The shift of the d−d band from 640 to 605 nm suggests the coordination of a third imidazole nitrogen, resulting in the $\{3N_{im}\}$ binding mode for the CuH_5L and CuH_4L species.

The coordination of an amide nitrogen occurs at pH above 5, as evidenced by the appearance of intense d−d bands in CD spectra (Figure 3). Interestingly, the CD spectra over the range 200−250 nm show that coordination of Cu^{2+} to the pHG peptide induces the appearance of two bands at 213 and 220 nm, suggesting the formation of an α-helical structure (Figure 4).[47,48]

At pH 5, a clear displacement of the maximum absorption in the direction of shorter wavelengths is observed in the UV−vis spectra (from 605 to 568 nm). The coordination of amide

DOI: 10.1021/acs.inorgchem.5b01029
Inorg. Chem. 2015, 54, 7692−7702

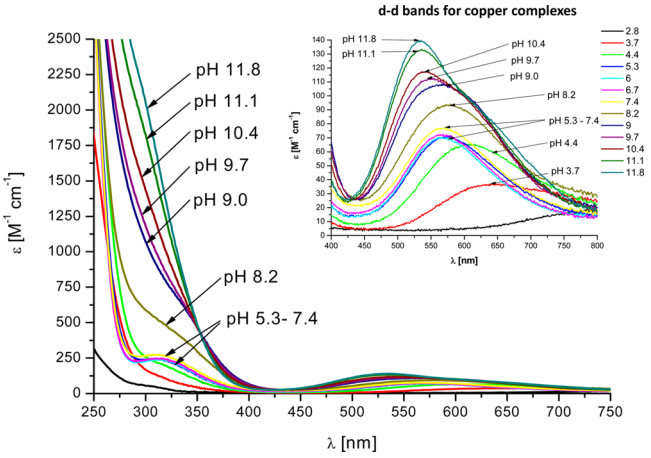

Figure 2. UV−vis absorption spectra at different pH values for the Cu^{2+}−pHG system in an aqueous solution of HCl at I = 0.1 mol·dm^{-3} (KCl) and 25 °C. $C_M^\circ = 4 \times 10^{-4}$ mol·dm^{-3}; M:L molar ratio = 1:1.1; path length = 1 cm.

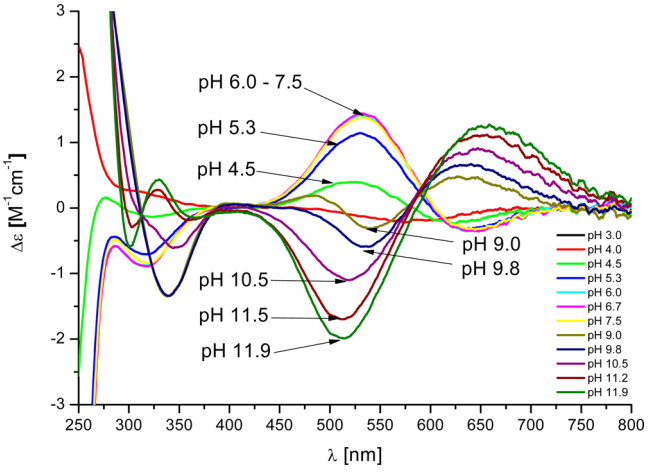

Figure 3. CD spectra at different pH values for the Cu^{2+}−pHG system in an aqueous solution of HCl at I = 0.1 mol·dm^{-3} (KCl) and 25 °C. $C_M^\circ = 4 \times 10^{-4}$ mol·dm^{-3}; M:L molar ratio = 1:1.1; path length = 1 cm.

nitrogen to Cu^{2+} is also supported by the increase intensity of the characteristic band at 313 nm (Figure 2).

Comparison of the experimental EPR spectra for the Cu^{2+}−pHG systems at pH 4.19 and 5.48 show pronounced differences (Figure S4). Especially the changes in the $A_{\parallel}$ and $g_{\parallel}$ parameters (Table 1) and the number of superhyperfine lines in the perpendicular region confirm the coordination of Cu^{2+} to the next nitrogen atom.

Deprotonation of the last His residue leads to the formation of CuL species. The {3N$_{im}$, N$^-$} coordination mode dominates to pH 8.5 (CuH_3L, CuH_2L, CuHL, CuL). The $N_{im} \rightarrow Cu^{2+}$ CD band at around 330 nm is observed at all pH values (Figure 3 and Table 1). In the alkaline pH range, amide nitrogens can effectively compete with imidazole nitrogens in binding to Cu^{2+}. The differences observed in the CD and UV−vis spectra support coordination with further amide nitrogens above pH 9. The coordination mode for $CuH_{-2}L$ is {2N$_{im}$, 2N$^-$} with a square-planar geometry. At pH above 10, the intensity of the d−d bands increases, and the differences in the d−d transition energy (i.e., a shift of the band to shorter wavelengths) indicate the coordination of the third amide nitrogen {N$_{im}$, 3N$^-$}. The 4N coordination is supported by the EPR parameters $A_{\parallel}$ from 187.5 to 194.9 G and $g_{\parallel}$ in the range 2.24−2.19 (Table 1).

The values of $A_{\parallel}$ and $g_{\parallel}$ strongly support the suggested coordination modes for the copper complexes.[1,49−54] The comparison of the numbers of superhyperfine lines for the systems at pH 4.19 and 5.48 (Figure S4) also supports the number of suggested nitrogen donors. Thus, three imidazole nitrogens participate in the binding at pH below 5, and an additional amide nitrogen binds at pH above 5.

Construction of Cu^{2+}−pHG Complexes for the MD Simulations. The computational study considered only imidazole groups of His that coordinate with Cu^{2+}. The computational study was based on the proposed hypothesis observed by the experimental study, in which the Cu^{2+} binds only to the His imidazole groups. Therefore, our initial structures illustrated Cu^{2+} binding only to imidazole groups. During the MD simulations and until the end of the simulations, the Cu^{2+} did not bind other amino acids of the peptide, such as Glu or Asp. This result indicates that the hypothesis that had been suggested by the experiments was correct. We previously showed that Cu^{2+} in the longer extended peptide $EDDH_9GVG_{10}$ binds not only to His but also to other amino acids such as Glu an Asp, although the initial structures showed interactions only of His imidazole groups with Cu^{2+}.[6] To date, the atomic structures of the pHG peptide and the

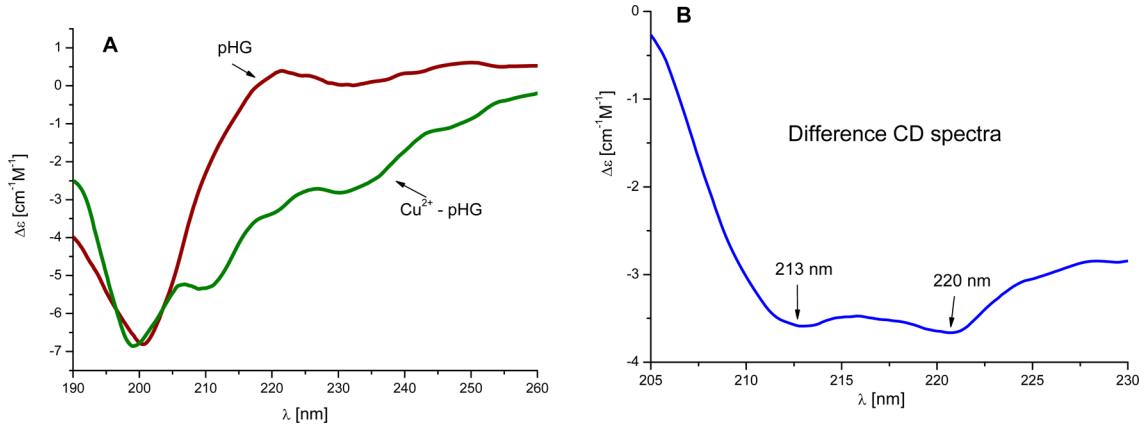

Figure 4. (A) CD spectra for pHG and the Cu^{2+}−pHG system and (B) the difference CD spectrum in aqueous solution at pH 5. $C_M^\circ = 4 \times 10^{-4}$ mol·dm^{-3}; M:L molar ratio = 1:1.1; path length = 0.01 cm.

DOI: 10.1021/acs.inorgchem.5b01029
Inorg. Chem. 2015, 54, 7692−7702

Cu^{2+}–pHG complex have not been solved using an experimental technique such as NMR spectroscopy or X-ray crystallography. The potentiometric measurements, UV–vis absorption spectra, and CD spectra suggest that imidazole groups coordinate with Cu^{2+} to form α-helical structures. We therefore constructed the initial structure of the pHG peptide as a helical structure. The modeling tools suggested that only when two consecutive His residues bind to Cu^{2+} does the peptide exhibit a helical structure. Furthermore, as shown below, the DFT calculations also suggested that binding to two consecutive His residues results in a helical structure. We then coordinated the Cu^{2+} ion to three histidines in various domains along the helical pHG peptide, forming the 12 different conformational models shown in Table 2. It is important to note that we chose the helical structure of pHG as the initial structure in the MD simulations to examine whether the helical structure would remain stable along the simulation for each model.

Table 2. Cu^{2+} Binding Sites (red) along the Sequence of pHG in Each Constructed Model

M1	Ac-EDD**HH**HH**H**HHHHG-NH_2
M2	Ac-EDDH**HH**HH**H**HHHG-NH_2
M3	Ac-EDDHH**HH**HH**H**HHG-NH_2
M4	Ac-EDDHHH**HH**HH**H**HG-NH_2
M5	Ac-EDDHHHH**HH**HH**H**G-NH_2
M6	Ac-EDD**H**HH**HH**HHHHG-NH_2
M7	Ac-EDDH**H**HH**HH**HHHG-NH_2
M8	Ac-EDDHH**H**HH**HH**HHG-NH_2
M9	Ac-EDDHHH**H**HH**HH**HG-NH_2
M10	Ac-EDDHHHH**H**HH**HH**G-NH_2
M11	Ac-EDDHHHHH**HH**HH**H**G-NH_2
M12	Ac-EDDH**H**HH**HH**HHHG-NH_2

To keep the helical structures, the following binding sites were examined. Models M1–M5 illustrate one group in which the "binding site template" involves two sequential histidines followed by a third histidine separated from them by two histidines. This binding site template is shifted along the sequence from the N-terminus to the C-terminus. Models M6–M10 illustrate a second group in which the binding site template involves one histidine followed by two sequential histidines separated from it by two histidines. This binding site template is also shifted along the sequence from the N-terminus to the C-terminus. Model M11 illustrates the binding site template of the first group (models M1–M5) but with only one histidine separating the three histidines, while model M12 illustrates the binding site template for the second group (models M6–M10) but with only one histidine separating the three histidines. The binding site of model M12 is similar to one of the models obtained from the DFT calculations.

The Cu^{2+}–pHG peptide is characterized by an α-helix structure with various conformations. The final simulated models M1–M12 are shown in Figure 5. The computed conformational energies and populations are listed in Table S1 in the Supporting Information. Interestingly, as shown in Figure 6, the populations of the first group (M1–M5) indicate that models in which the binding site template is closer to the N- or the C-terminal domain (M1, M4, and M5) are relatively more favored than those in which the binding site template is located in the middle of the sequence (M2 and M3). The models in the second group (M6–M10) exhibited similar populations. M11 and M12 are also favored. We therefore conclude that there is a polymorphism, indicating that Cu^{2+} can bind in several domains along the pHG peptide, with a slight preference for binding to the C- and N- terminal domains of the peptide.

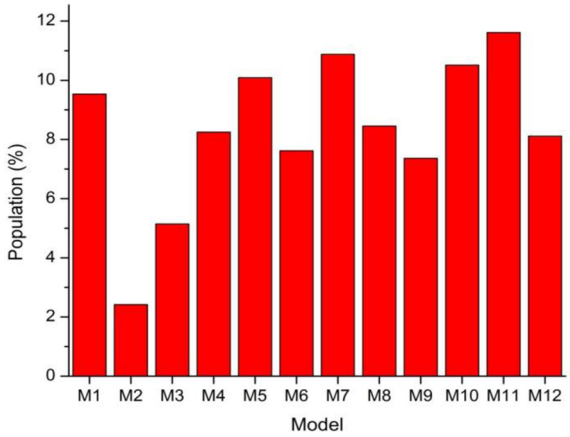

Figure 6. Populations of models M1–M12 obtained from GBMV and Monte Carlo calculations.

The DSSP analysis of the secondary structure revealed that all of the models show α-helix domains along the sequence (Figure 7 and Figures S5 and S6). In the first group, model M1 shows properties of a regular α-helix, while in models M2 and M3 (where the binding site is located in the middle region of the peptide) the regular helical properties "disappear" in the N-terminal and C-terminal domains, respectively. It is important to note that according to the DSSP calculations (Figure 7), the helical structure all along the sequence of model M3 disappears. In models M4 and M5, in which the binding site template is more located in the C-terminal region of the peptide, the

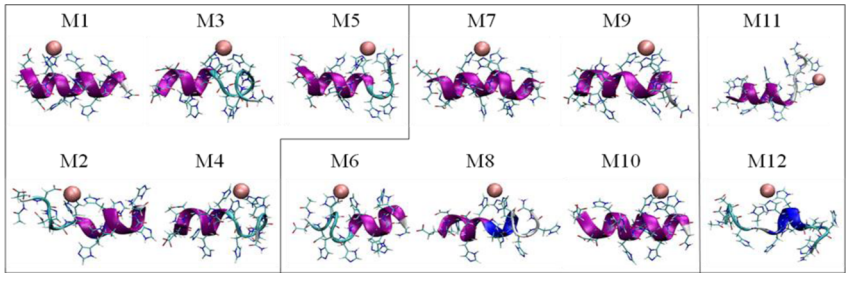

Figure 5. Final simulated Cu^{2+}–pHG complexes demonstrating α-helical structures. The helical structural properties were obtained according to the STRIDE algorithm (which is implemented in VMD). The colors of the backbone indicate the secondary structure of the peptide: regular α-helix (purple), 3_{10} helix (blue), turn (cyan), and coil (white).

DOI: 10.1021/acs.inorgchem.5b01029
Inorg. Chem. 2015, 54, 7692–7702

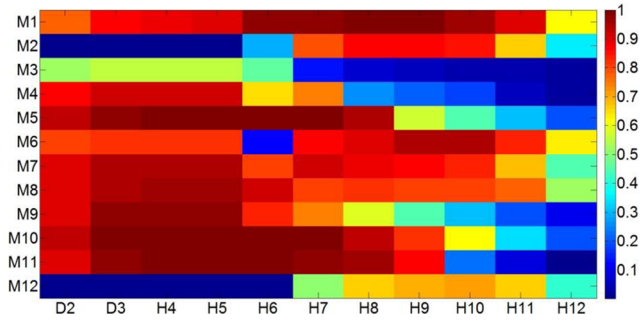

Figure 7. DSSP calculations for each residue along the pHG peptide for each model. The value for each residue is the average value obtained from 30 ns of the simulation. Red indicates a regular α-helix, while other colors indicate other structures (disordered regions or loops).

regular helical properties "disappear" in the C-terminal domains.

In the second group, models M6, M7, and M8 demonstrate regular properties of an α-helix according to the DSSP calculations. However, according to the STRIDE calculations, model M6 has a turn in the N-terminal domain, and model M8 has 3_{10} helix and a coil in the C-terminal domain (Figure 5). In models M9 and M10, in which the binding site template is more located in the C-terminal region of the peptide, DSSP shows that the helical properties disappear in the C-terminal domains (a similar scenario as for models M4 and M5), but according to the STRIDE calculations, M9 and M10 show a regular α-helix. In model M11, which has a similar binding site template as the first group (models M1−M5) but with only one histidine separating the histidines that bind the Cu^{2+}, the three His residues in the C-terminal region have no regular helical properties according to DSSP. However, the STRIDE calculations show a regular α-helix in the N-terminal domain and a coil in the C-terminal domain that binds the Cu^{2+}. Finally, in model M12, in which has a similar binding site template as the second group (models M6−M10) but with only one histidine separating the histidines that bind the Cu^{2+}, the regular helical properties for all of the residues disappear. This is also in agreement with the STRIDE calculations, which indicate that model M12 has 3_{10} helix properties (Figure 5). In summary, the MD simulations showed that all of the models have properties of a regular α-helix or 3_{10} helix. These results are in agreement with the observations from the CD measurements.

DFT calculations were performed on three multiply connected 1:1 complexes (Figure 8). The computed free

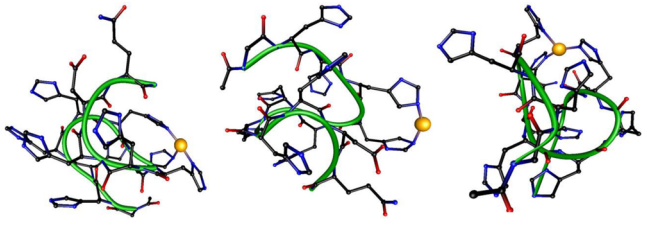

Figure 8. DFT-optimized structures of Cu^{2+}−pHG complexes. In complex A (left), the Cu^{2+} binds to His9, His10, and His11. In complex B (middle), the Cu^{2+} binds to His7 and His8. In complex C (right), the Cu^{2+} binds to His5, His7, and His8. Complex C is similar to model M12 (Figure 5). Green tubes follow the backbones.

pHG peptide provides three domains in which three imidazoles can bind Cu^{2+} to form Cu^{2+}−pHG complexes. The least energetically stable complex among these three complexes is complex B (Figure 8). In complex B, the Cu^{2+} ion is bound to two imidazoles. We previously showed that Cu^{2+} binds to two imidazoles in the His_6 tag peptide.[1] In the present case, the pHG is a longer peptide consisting of nine histidine residues, and therefore, most of the histidines do not participate in the coordination with the Cu^{2+}. However, the presence of multiple numbers of histidine residues allows the formation of an extensive network of hydrogen bonds that stabilizes the Cu^{2+}−pHG complexes. The hydrogen-bonding network is crucial for the formation of the secondary structure and contributes to overwhelm the backbone energy and consequently stabilize the structure of the Cu^{2+}−pHG complex.

Complexes A and C (Figure 8) are energetically the most stable structures. In both complex A and complex C, three imidazole groups bind to Cu^{2+}. The relative energies (0.0 < 11.49 < 15.71 kcal/mol for C, A, and B, respectively) indicate that the pHG peptide prefers to interact with three rather than two imidazole groups. Considering all three complexes, excluding the C- and N-terminal histidines in the pHG peptide, His6 is the only residue that does bind Cu^{2+}. All three complexes showed 6−10 hydrogen bonds (Figure S7) and a 3_{10} helix or a regular α-helix, which is a typical structural motif as observed elsewhere.[55] For example, complex A exhibits cooperative chains of hydrogen bonds that contribute to the stability. It is known that such cooperative chains of hydrogen bonds contribute to the stability of a monomer more than in the dimer form.[56]

In summary, the folding of the free pHG peptide allows several Cu^{2+} binding sites. The investigated Cu^{2+}−pHG peptide complexes are very stable because of the strong cation−imidazole interaction and the hydrogen-bonding network that forms α-helical structures. The intramolecular hydrogen bonds contribute to the cooperative chains that contribute to the complex stability. In all of the complexes, we found regular α-helix and typical 3_{10} helix structures, as previously shown elsewhere.[55]

Investigation of the Effect of Different Metal Ions on the pHG Peptide. *Ni^{2+}−pHG Complexes.* The titration curves for Ni^{2+}−pHG complexes fit best to the formation of the following complexes at pH below 6: NiH_7L, NiH_6L, NiH_4L, NiHL, and NiL (Figure 9). The potentiometric study could be not conducted at pH higher than 6 because of precipitation of the complex. Thus, only side-chain binding may occur in the species mentioned above. The pK_a of 4.63 for $NiH_7L \rightarrow NiH_6L$ suggests binding of the third imidazole nitrogen to the Ni^{2+} ion (Table 3). The pHG peptide forms only equimolar complexes with Ni^{2+} at m/z 883.3 (for $[NiL]^{2+}$) and m/z 589.2 (for $[NiL]^{3+}$) (Figure S8). The experimental and simulated ESI-MS signals are in perfect agreement and all are equimolar. The proposed binding modes are shown in Table 3.

Above pH 9 the complex was again soluble, allowing spectroscopic studies to be conducted. The CD and UV−vis spectra for the Ni^{2+} complexes suggest coordination of the amide nitrogen at pH higher than 9.6. The absorbance maximum at 420−500 nm in the UV−vis and CD spectra at pH 10−11 (Figures 10 and 11) could be due to the coordination of an amide nitrogen, resulting in the formation of square-planar Ni^{2+} complexes.

Zn^{2+}−pHG Complexes. The formation of zinc complexes starts at higher pH with respect to the copper and nickel ones

DOI: 10.1021/acs.inorgchem.5b01029
Inorg. Chem. 2015, 54, 7692−7702

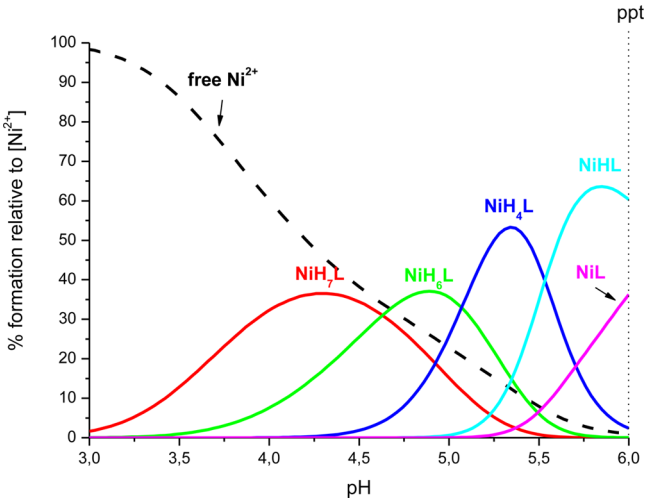

Figure 9. Representative distribution diagram for the formation of Ni^{2+}–pHG complexes at 25 °C and I = 0.1 mol·dm^{-3} (KCl). $C_M^\circ = 4 \times 10^{-4}$ mol·dm^{-3}; M:L molar ratio = 1:1.1.

Table 3. Proposed Binding Modes for Ni^{2+} complexes

species	log β^a	pK_a	proposed donors
NiH_7L	48.81(6)		$2N_{im}$
NiH_6L	44.18(4)	4.63	$3N_{im}$
NiH_4L	34.04(4)		$3N_{im}$
NiHL	17.44(3)		$3N_{im}$
NiL	11.22(6)	6.22	$3N_{im}$

[a]Standard deviations in the last figure are shown in parentheses.

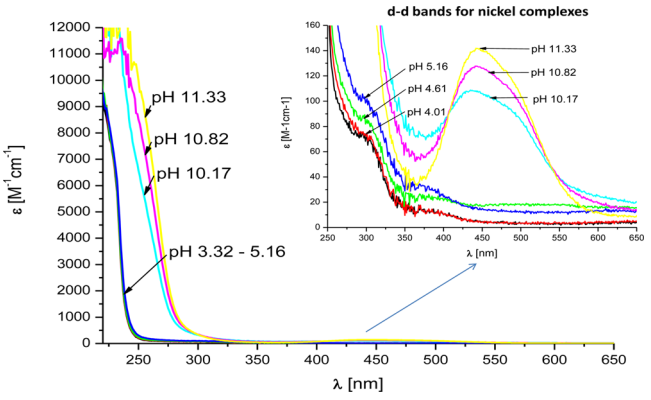

Figure 10. UV–vis absorption spectra at different pH values for the Ni^{2+}–pHG system in an aqueous solution of HCl at I = 0.1 mol·dm^{-3} (KCl) and 25 °C. $C_M^\circ = 4 \times 10^{-4}$ mol·dm^{-3}; M:L molar ratio = 1:1.1; path length = 1 cm.

(at pH 3.5). The potentiometric titrations were not possible at pH above 6.5 because of precipitation (Figure 12). The Zn^{2+} complex formation constants are shown in Table 4. The ESI-MS measurements revealed the stoichiometry of the zinc complexes, indicating that only equimolar species were present in the solution (Figure S9). The similar stability constants for particular species of Ni^{2+} and Zn^{2+} may indicate similar binding modes in these two cases. The first complex, ZnH_6L, with maximum concentration at pH 4.6, suggests that three imidazole residues are coordinated to the zinc ion. The other complexes can have the same coordination donors.

Effect of the Type of Divalent Metal Ion on the Bond Lengths of Metal–Imidazole Groups. To examine the

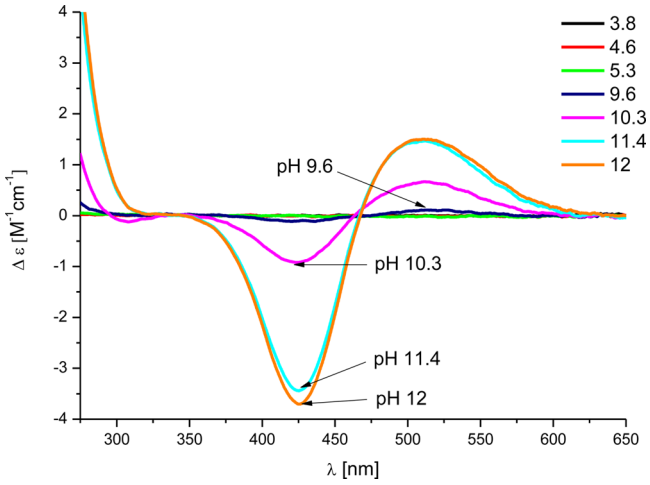

Figure 11. CD spectra at different pH values for the Ni^{2+}–pHG system in an aqueous solution of HCl at I = 0.1 mol·dm^{-3} (KCl) and 25 °C. $C_M^\circ = 4 \times 10^{-4}$ mol·dm^{-3}; M:L molar ratio = 1:1.1; path length = 1 cm.

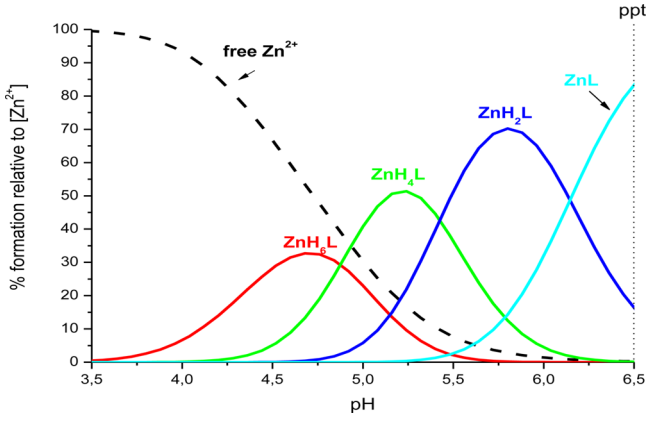

Figure 12. Representative distribution diagram for the formation of Zn^{2+}–pHG complexes at 25 °C and I = 0.1 mol·dm^{-3} (KCl). $C_M^\circ = 4 \times 10^{-4}$ mol·dm^{-3}; M:L molar ratio = 1:1.1.

Table 4. Formation Constants of Zn^{2+}–pHG complexes at 25 °C and I = 0.1 mol·dm^{-3} (KCl)

species	log β^a	proposed donors
ZnH_6L	43.74(2)	$3N_{im}$
ZnH_4L	33.99(1)	$3N_{im}$
ZnH_2L	23.14(1)	$3N_{im}$
ZnL	10.85(1)	$3N_{im}$

[a]Standard deviations in the last figure are shown in parentheses.

effect of the type of the divalent metal ion on the metal–imidazole bond length, we bound Zn^{2+} and Ni^{2+} to similar binding sites as in the Cu^{2+}–pHG complexes as shown in Figure 8. All of the studied metal ions bind to imidazole nitrogens. The ranges of bond lengths are 1.865–2.098 Å, 1.848–2.652 Å, and 1.990–2.732 Å for Ni^{2+}, Cu^{2+}, and Zn^{2+}, respectively (Table 5). Interestingly, Cu^{2+} has the shortest metal–peptide bond length (1.848 Å) among all of the divalent metal ions. Furthermore, the Cu^{2+}–imidazole bond lengths in complexes B and C demonstrate a shorter average metal–peptide bond compared with complex A. However, the differences in the bond lengths are small. For Cu^{2+}–N(His), the distance range is 1.848–2.652 Å (Table 5). In metal-

DOI: 10.1021/acs.inorgchem.5b01029
Inorg. Chem. 2015, 54, 7692–7702

Table 5. Metal Ion−N_{im} Bond Distances (Å) and Angles (deg) Computed by DFT

distance/angle	Ni^{2+}	Cu^{2+}	Zn^{2+}
Complex A			
M^{2+}−N(His9)	1.906	1.850	2.260
M^{2+}−N(His10)	2.098	2.652	2.104
M^{2+}−N(His11)	1.905	1.854	2.073
N(His9)−M^{2+}−N(His10)	98.6	100.4	89.5
N(His10)−M^{2+}−N(His11)	94.6	86.8	89.7
N(His9)−M^{2+}−N(His11)	158.3	167.4	114.1
Complex B			
M^{2+}−N(His7)	1.888	1.848	2.075
M^{2+}−N(His8)	1.865	1.871	2.027
N(His_9)−M^{2+}−N(His_{10})	137.7	147.8	93.9
Complex C			
M^{2+}−N(His5)	1.912	2.230	2.096
M^{2+}−N(His7)	1.986	1.882	1.990
M^{2+}−N(His8)	1.921	1.864	2.732
N(His5)−M^{2+}−N(His7)	102.4	103.2	90.2
N(His7)−M^{2+}−N(His8)	102.2	156.4	91.8
N(His5)−M^{2+}−N(His8)	155.0	100.4	177.2

loproteins, this distance is suggested to be 1.79−2.04 Å.[57] In the MD and MC simulations, the most probable distances are in the range 2.15−2.35 Å (for an example, see Figure S10). The distance observed in the MD and MC simulations is expected to be higher than that listed in bioinorganic chemistry textbooks, since the temperature at which the simulations were performed was 310 K rather than 0 K. The metal−peptide complex is dynamic and flexible and not a rigid, frozen structure, and thus, it is expected that these distances are slightly higher than the literature values.

As shown in above and in our previous work,[1,6] the peptide forms equimolar complexes with ions. The metal ion binds to nitrogens from imidazole rings of histidine residues. The DFT results show that analogous complexes with the divalent metal ions Ni^{2+}, Cu^{2+}, and Zn^{2+} do not have dramatically different metal−imidazole bond lengths and that these complexes have similar structures. The backbone of the peptide and the binding site do not change upon complexation of different ions. Our previous work supports this observation.[58] The metal−imidazole bond lengths in most cases correspond to the ionic radii (Ni^{2+} < Cu^{2+} < Zn^{2+}),[59] with the exception of open-shell Cu^{2+}, which makes shorter distances and the most effective bonds in comparison with other investigated metal ions, as previously shown by various experimental techniques.[60]

The competition plot shows the ability of pHG to bind the various divalent metal ions Cu^{2+}, Ni^{2+}, and Zn^{2+} (Figure 13). This plot indicates that the most effective binding occurs for Cu^{2+}. The DFT calculations provide an interpretation of these results that is related to the relatively short Cu^{2+}−imidazole distances (compared with those for the two other metal ions), which stabilize this complex.

The DFT calculations clearly show that for Cu^{2+}, Ni^{2+}, and Zn^{2+} ions, the impact of metal exchange on the entire complex structure is negligible. The complexes of all of these metal ions have extended stabilizing networks of hydrogen bonds. All of the complexes contain helical fragments with bifurcated hydrogen bonds typical both for 3_{10} helix and regular α-helix structures.

Protection of the N-terminus of the peptide distinctly decreases the binding ability of pHG compared with the N-terminal amino nitrogen in the wild-type venom pHpG-1 peptide[6] (Figure 14). This clearly indicates the involvement of

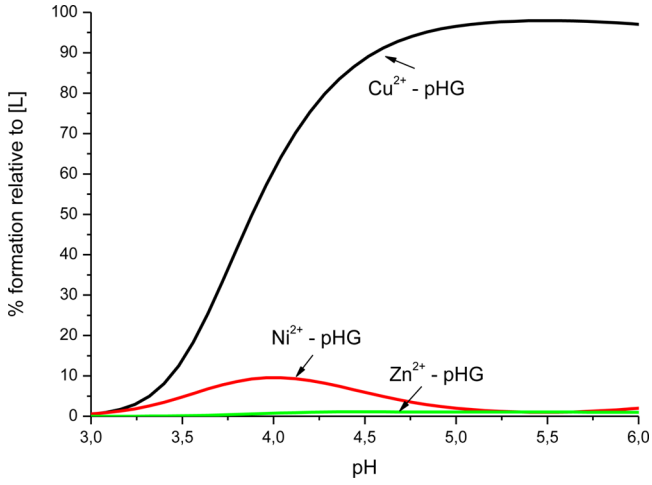

Figure 13. Competition plot for Cu^{2+}, Ni^{2+}, and Zn^{2+} with pHG peptide at pH values below those where precipitation of nickel and zinc complexes occurs.

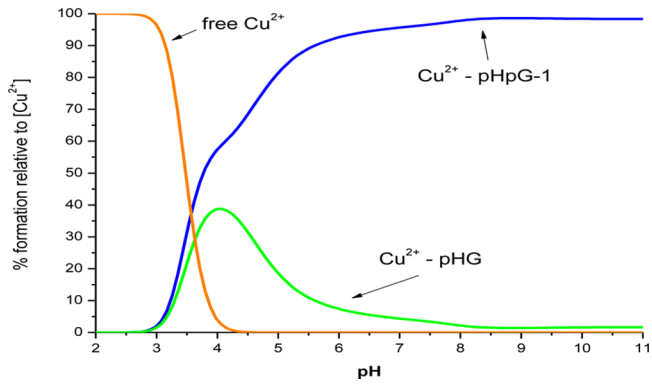

Figure 14. Competition plot for Cu^{2+}−pHG and Cu^{2+}−pHpG-1[6] complexes.

metal ion binding. Interestingly, the protected pHG peptide studied here is a better ligand for Cu^{2+} than the protected His_6 peptide[1] (Figure 15). This supports the involvement of three imidazole nitrogens in the case of pHG. The results obtained here indicate the high affinity for metal ion binding and the

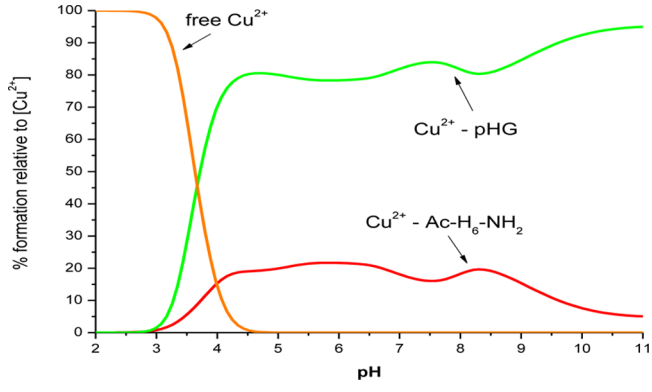

Figure 15. Competition plot for Cu^{2+}−pHG and Cu^{2+}−His_6[1] complexes.

DOI: 10.1021/acs.inorgchem.5b01029
Inorg. Chem. 2015, 54, 7692−7702

strong impact of metal ion coordination on the structure of histidine tags. Also, in the case of Ni^{2+} and Zn^{2+} ions, the coordination to a His tag is very effective, as seen in comparisons with histidine-rich peptides (Figures 16 and 17).

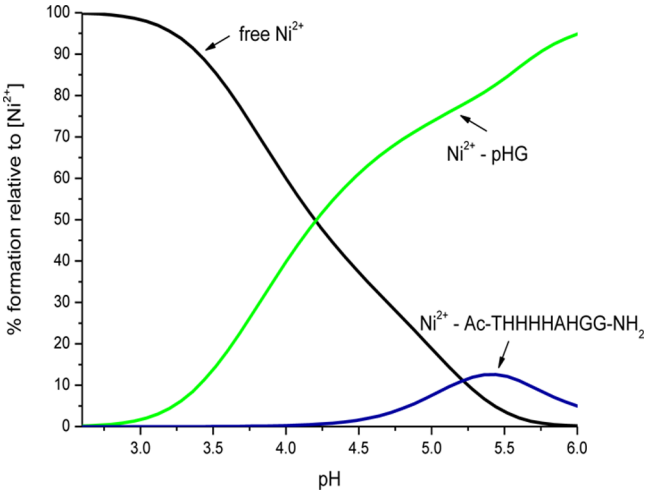

Figure 16. Competition plot for Ni^{2+}–pHG and Ni^{2+}–Ac-THHHHAHGG-NH_2[61] complexes.

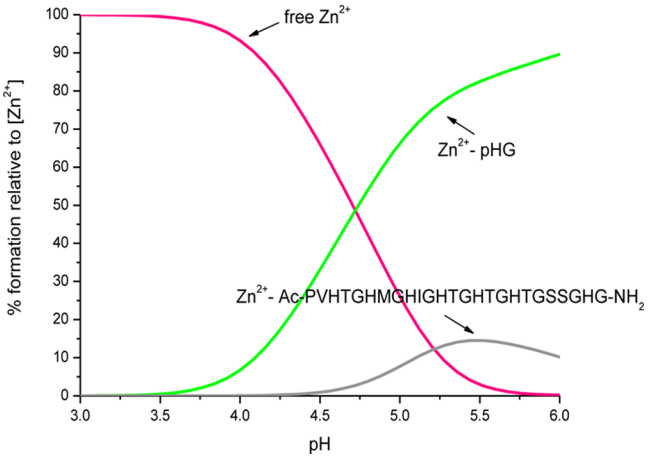

Figure 17. Competition plot for Zn^{2+}–pHG and Zn^{2+}–Ac-PVHTGHMGHIGHTGHTGHTGSSGHG-NH_2[62] complexes.

It should also be underlined that histidine tags serve as polymorphic binding sites, allowing metal ions to move along the peptide chain; such complexes form helical structures with specific hydrogen-bonding networks.

CONCLUSIONS

This work has demonstrated that divalent metal ions such as Cu^{2+}, Ni^{2+}, and Zn^{2+} can efficiently bind to the polyhistidine fragment of pHG, a peptide derived from an African viper. CD spectroscopy and computational studies showed that the metal–pHG complex has an α-helical structure of a 3_{10} helix stabilized by a hydrogen-bonding network. Interestingly, because there are multiple His residues along this pHG peptide, the metal ions can bind in various domains along the sequence and therefore form polymorphic states, similar to those observed for a His_6 tag. In the present case, the peptide has nine His residues and is thus able to exist in more polymorphic states. Furthermore, while the His_6 tag showed a slight preference for an α-helix-like structure, the His_9-containing peptide studied in this work is a regular α-helix. Future studies are necessary to examine whether the elongation of the metal-bound poly-His tag may affect the formation of secondary structures.

ASSOCIATED CONTENT

Supporting Information

Figures S1–S12, Table S1, and Cartesian coordinates for the complexes (TXT). The Supporting Information is available free of charge on the ACS Publications website at DOI: 10.1021/acs.inorgchem.5b01029.

AUTHOR INFORMATION

Corresponding Authors

*H.K.: E-mail: henryk.kozlowski@chem.uni.wroc.pl. Tel: (+48) (71) 375 72 51. Fax: (+48) (71) 375 72 51.

*Y.M.: E-mail: ymiller@bgu.ac.il. Tel: 972-86428705. Fax: 972-86428709.

Notes

The authors declare no competing financial interest.

ACKNOWLEDGMENTS

Financial support from the Polish Ministry of Science and Higher Education (4478/E-344/S/2014) and from the project "Academy of Development as the Key To Strengthen Human Resources of the Polish Economy" cofinanced by the European Union under the European Social Fund is acknowledged. This research was partially supported by Grant 2011128 from the United States–Israel Binational Science Foundation (BSF). All of the simulations were performed using the high-performance computational facilities of the Miller lab in the BGU HPC computational center. The support of the BGU HPC computational center staff is greatly appreciated.

REFERENCES

(1) Watly, J.; Simonovsky, E.; Wieczorek, R.; Barbosa, N.; Miller, Y.; Kozlowski, H. *Inorg. Chem.* **2014**, *53*, 6675–6683.
(2) Waugh, D. S. *Trends Biotechnol.* **2005**, *23*, 316–320.
(3) Witkowska, D.; Rowinska-Zyrek, M.; Valensin, G.; Kozlowski, H. *Coord. Chem. Rev.* **2012**, *256*, 133–148.
(4) Salichs, E.; Ledda, A.; Mularoni, L.; Albà, M. M.; de la Luna, S. *PLoS Genet.* **2009**, *5* (3), e1000397.
(5) Favreau, P.; Cheneval, O.; Menin, L.; Michalet, S.; Gaertner, H.; Principaud, F.; Thai, R.; Menez, A.; Bulet, P.; Stocklin, R. *Rapid Commun. Mass Spectrom.* **2007**, *21*, 406–412.
(6) Pontecchiani, F.; Simonovsky, E.; Wieczorek, R.; Barbosa, N.; Rowinska-Zyrek, M.; Potocki, S.; Remelli, M.; Miller, Y.; Kozlowski, H. *Dalton Trans.* **2014**, *43*, 16680–16689.
(7) Wagstaff, S. C.; Favreau, P.; Cheneval, O.; Laing, G. D.; Wilkinson, M. C.; Miller, R. L.; Stöcklin, R.; Harrison, R. A. *Biochem. Biophys. Res. Commun.* **2008**, *365*, 650–656.
(8) Atherton, E.; Sheppard, R. C. *Solid Phase Peptide Synthesis: A Practical Approach*; Oxford University Press: New York, 1989.
(9) Fields, G. B.; Noble, R. L. *Int. J. Pept. Protein Res.* **1990**, *35*, 161–214.
(10) Irving, H. M.; Miles, M. G.; Pettit, L. D. *Anal. Chim. Acta* **1967**, *38*, 475–485.
(11) Gran, G. *Acta Chem. Scand.* **1950**, *4*, 559–577.
(12) Gans, P.; Sabatini, A.; Vacca, A. *J. Chem. Soc., Dalton Trans.* **1985**, 1195–1200.
(13) Gans, P.; Sabatini, A.; Vacca, A. *Talanta* **1996**, *43*, 1739–1753.
(14) Alderighi, L.; Gans, P.; Ienco, A.; Peters, D.; Sabatini, A.; Vacca, A. *Coord. Chem. Rev.* **1999**, *184*, 311–318.

DOI: 10.1021/acs.inorgchem.5b01029
Inorg. Chem. 2015, 54, 7692–7702

(15) Wineman-Fisher, V.; Simkovitch, R.; Shomer, S.; Gepshtein, R.; Huppert, D.; Saif, M.; Kallio, K.; Remington, S. J.; Miller, Y. *Phys. Chem. Chem. Phys.* **2014**, *16*, 11211−11223.
(16) Zeytuni, N.; Uebe, R.; Maes, M.; Davidov, G.; Baram, M.; Raschdorf, O.; Nadav-Tsubery, M.; Kolusheva, S.; Bitton, R.; Goobes, G.; Friedler, A.; Miller, Y.; Schüler, D.; Zarivach, R. *PLoS One* **2014**, *9*, e92141.
(17) Raz, Y.; Rubinov, B.; Matmor, M.; Rapaport, H.; Ashkenasy, G.; Miller, Y. *Chem. Commun.* **2013**, *49*, 6561−6563.
(18) Raz, Y.; Miller, Y. *PLoS One* **2013**, *8*, e73303.
(19) Raz, Y.; Adler, J.; Vogel, A.; Scheidt, H. A.; Haupl, T.; Abel, B.; Huster, D.; Miller, Y. *Phys. Chem. Chem. Phys.* **2014**, *16*, 7710−7717.
(20) Wineman-Fisher, V.; Atsmon-Raz, Y.; Miller, Y. *Biomacromolecules* **2015**, *16*, 156−165.
(21) Miller, Y.; Ma, B. Y.; Nussinov, R. *Coord. Chem. Rev.* **2012**, *256*, 2245−2252.
(22) Kale, L.; Skeel, R.; Bhandarkar, M.; Brunner, R.; Gursoy, A.; Krawetz, N.; Phillips, J.; Shinozaki, A.; Varadarajan, K.; Schulten, K. *J. Comput. Phys.* **1999**, *151*, 283−312.
(23) MacKerell, A. D.; Bashford, D.; Bellott, M.; Dunbrack, R. L.; Evanseck, J. D.; Field, M. J.; Fischer, S.; Gao, J.; Guo, H.; Ha, S.; Joseph-McCarthy, D.; Kuchnir, L.; Kuczera, K.; Lau, F. T. K.; Mattos, C.; Michnick, S.; Ngo, T.; Nguyen, D. T.; Prodhom, B.; Reiher, W. E.; Roux, B.; Schlenkrich, M.; Smith, J. C.; Stote, R.; Straub, J.; Watanabe, M.; Wiorkiewicz-Kuczera, J.; Yin, D.; Karplus, M. *J. Phys. Chem. B* **1998**, *102*, 3586−3616.
(24) Brooks, B. R.; Bruccoleri, R. E.; Olafson, B. D.; States, D. J.; Swaminathan, S.; Karplus, M. *J. Comput. Chem.* **1983**, *4*, 187−217.
(25) Miller, Y.; Ma, B.; Nussinov, R. *Proc. Natl. Acad. Sci. U. S. A.* **2010**, *107*, 9490−9495.
(26) Parthasarathy, S.; Long, F.; Miller, Y.; Xiao, Y.; McElheny, D.; Thurber, K.; Ma, B.; Nussinov, R.; Ishii, Y. *J. Am. Chem. Soc.* **2011**, *133*, 3390−3400.
(27) Zeytuni, N.; Uebe, R.; Maes, M.; Davidov, G.; Baram, M.; Raschdorf, O.; Friedler, A.; Miller, Y.; Schüler, D.; Zarivach, R. *PLoS One* **2014**, *9*, No. e97154.
(28) Mahoney, M. W.; Jorgensen, W. L. *J. Chem. Phys.* **2000**, *112*, 8910−8922.
(29) Jorgensen, W. L.; Chandrasekhar, J.; Madura, J. D.; Impey, R. W.; Klein, M. L. *J. Chem. Phys.* **1983**, *79*, 926−935.
(30) Tu, K.; Tobias, D. J.; Klein, M. L. *Biophys. J.* **1995**, *69*, 2558−2562.
(31) Feller, S. E.; Zhang, Y. H.; Pastor, R. W.; Brooks, B. R. *J. Chem. Phys.* **1995**, *103*, 4613−4621.
(32) Essmann, U.; Perera, L.; Berkowitz, M. L.; Darden, T.; Lee, H.; Pedersen, L. G. *J. Chem. Phys.* **1995**, *103*, 8577−8593.
(33) Darden, T.; York, D.; Pedersen, L. *J. Chem. Phys.* **1993**, *98*, 10089−10092.
(34) Ryckaert, J. P.; Ciccotti, G.; Berendsen, H. J. C. *J. Comput. Phys.* **1977**, *23*, 327−341.
(35) Lee, M. S.; Salsbury, F. R.; Brooks, C. L. *J. Chem. Phys.* **2002**, *116*, 10606−10614.
(36) Lee, M. S.; Feig, M.; Salsbury, F. R.; Brooks, C. L. *J. Comput. Chem.* **2003**, *24*, 1348−1356.
(37) Kabsch, W.; Sander, C. *Biopolymers* **1983**, *22*, 2577−2637.
(38) Frishman, D.; Argos, P. *Proteins: Struct., Funct., Genet.* **1995**, *23*, 566−579.
(39) Humphrey, W.; Dalke, A.; Schulten, K. *J. Mol. Graphics* **1996**, *14*, 33−38.
(40) Pait, M.; Shatruk, M.; Lengyel, J.; Gomez-Coca, S.; Bauza, A.; Frontera, A.; Bertolasi, V.; Ray, D. *J. Chem. Soc., Dalton Trans.* **2015**, *44*, 6107−6117.
(41) Latajka, Z.; Mielke, Z.; Olbert-Majkut, A.; Wieczorek, R.; Tokhadze, K. G. *Phys. Chem. Chem. Phys.* **1999**, *1*, 2441−2448.
(42) Gorelsky, S. I.; Basumallick, L.; Vura-Weis, J.; Sarangi, R.; Hodgson, K. O.; Hedman, B.; Fujisawa, K.; Solomon, E. I. *Inorg. Chem.* **2005**, *44*, 4947−4960.
(43) Frisch, M. J.; Trucks, G. W.; Schlegel, H. B.; Scuseria, G. E.; Robb, M. A.; Cheeseman, J. R.; Scalmani, G.; Barone, V.; Mennucci, B.; Petersson, G. A.; Nakatsuji, H.; Caricato, M.; Li, X.; Hratchian, H. P.; Izmaylov, A. F.; Bloino, J.; Zheng, G.; Sonnenberg, J. L.; Hada, M.; Ehara, M.; Toyota, K.; Fukuda, R.; Hasegawa, J.; Ishida, M.; Nakajima, T.; Honda, Y.; Kitao, O.; Nakai, H.; Vreven, T.; Montgomery, J. A., Jr.; Peralta, J. E.; Ogliaro, F.; Bearpark, M.; Heyd, J. J.; Brothers, E.; Kudin, K. N.; Staroverov, V. N.; Kobayashi, R.; Normand, J.; Raghavachari, K.; Rendell, A.; Burant, J. C.; Iyengar, S. S.; Tomasi, J.; Cossi, M.; Rega, N.; Millam, J. M.; Klene, M.; Knox, J. E.; Cross, J. B.; Bakken, V.; Adamo, C.; Jaramillo, J.; Gomperts, R.; Stratmann, R. E.; Yazyev, O.; Austin, A. J.; Cammi, R.; Pomelli, C.; Ochterski, J. W.; Martin, R. L.; Morokuma, K.; Zakrzewski, V. G.; Voth, G. A.; Salvador, P.; Dannenberg, J. J.; Dapprich, S.; Daniels, A. D.; Farkas, Ö.; Foresman, J. B.; Ortiz, J. V.; Cioslowski, J.; Fox, D. J. *Gaussian 09*; Gaussian, Inc.: Wallingford, CT, 2009.
(44) Zhao, Y.; Truhlar, D. G. *Theor. Chem. Acc.* **2008**, *120*, 215−241.
(45) Peisach, J.; Blumberg, W. E. *Arch. Biochem. Biophys.* **1974**, *165*, 691−708.
(46) Matera, A.; Brasun, J.; Cebrat, M.; Swiatek-Kozłowska, J. *Polyhedron* **2008**, *27*, 1539−1555.
(47) Brown, D. R.; Guantieri, V.; Grasso, G.; Impellizzeri, G.; Pappalardo, G.; Rizzarelli, E. *J. Inorg. Biochem.* **2004**, *98*, 133−143.
(48) Nicoll, A. J.; Miller, D. J.; Futterer, K.; Ravelli, R.; Allemann, R. K. *J. Am. Chem. Soc.* **2006**, *128*, 9187−9193.
(49) Pettit, L. D.; Gregor, J. E.; Kozlowski, H. Complex Formation between Metal Ions and Peptides. In *Perspectives on Bioinorganic Chemistry*; Hay, R. W., Dilworth, J. R., Nolan, K. B., Eds.; JAI Press: London, 1991; Vol. *1*, pp 1−41.
(50) Kowalik-Jankowska, T.; Kozlowski, H.; Farkas, E.; Sovago, I. Nickel Ion Complexes of Amino Acids and Peptides. In *Metal Ions in Life Sciences*; Sigel, A., Sigel, H., Sigel, R. K. O., Eds.; Wiley & Sons: Chichester, U.K., 2007; Vol. *2*, pp 63−108.
(51) Gaggelli, E.; Jankowska, E.; Kozlowski, H.; Marcinkowska, A.; Migliorini, C.; Stanczak, P.; Valensin, D.; Valensin, G. *J. Phys. Chem. B* **2008**, *112*, 15140−15150.
(52) Witkowska, D.; Valensin, D.; Rowinska-Zyrek, M.; Karafova, A.; Kamysz, W.; Kozlowski, H. *J. Inorg. Biochem.* **2012**, *107*, 73−81.
(53) Kowalik-Jankowska, T.; Ruta-Dolejsz, M.; Wisniewska, K.; Łankiewicz, L.; Kozłowski, H. *J. Chem. Soc., Dalton Trans.* **2000**, 4511−4519.
(54) Kowalski, J. M.; Bennett, B. *J. Am. Chem. Soc.* **2011**, *133*, 1814−1823.
(55) Wieczorek, R.; Dannenberg, J. J. *J. Am. Chem. Soc.* **2004**, *126*, 14198−14205.
(56) Kobko, N.; Dannenberg, J. J. *J. Phys. Chem. A* **2003**, *107*, 10389−10395.
(57) Hussain Reddy, K. *Bioinorganic Chemistry*; New Age International (P) Limited: New Delhi, India, 2003.
(58) Janicka-Klos, A.; Porciatti, E.; Valensin, D.; Conato, C.; Remelli, M.; Oldziej, S.; Valensin, G.; Kozlowski, H. *Dalton Trans.* **2013**, *42*, 448−458.
(59) Shannon, R. D. *Acta Crystallogr., Sect. A: Cryst. Phys., Diffr., Theor. Gen. Crystallogr.* **1976**, *32*, 751−767.
(60) Potocki, S.; Valensin, D.; Kozlowski, H. *Dalton Trans.* **2014**, *43*, 10215−10223.
(61) Witkowska, D.; Politano, R.; Rowinska-Zyrek, M.; Guerrini, R.; Remelli, M.; Kozlowski, H. *Chem. - Eur. J.* **2012**, *18*, 11088−11099.
(62) Szyrwiel, L.; Jankowska, E.; Janicka-Klos, A.; Szewczuk, Z.; Valensin, D.; Kozlowski, H. *Dalton Trans.* **2008**, 6117−6120.

DOI: 10.1021/acs.inorgchem.5b01029
Inorg. Chem. 2015, 54, 7692−7702